EUROPEAN PHYSICAL JOURNAL PLUS

ACCEPTED OCTOBER 20TH 2021

Numerical study of axisymmetric magneto-gyrotactic bioconvection in non-Fourier tangent hyperbolic nano-functional reactive coating flow of a cylindrical body in porous media

G. Kumaran[1], R. Sivaraj[1,a], V. Ramachandra Prasad[1], O. Anwar Beg[2], Ho-Hon Leung[3], and F. Kamalov[4]

[1] Department of Mathematics, School of Advanced Sciences, Vellore Institute of Technology, Vellore, India 632014.
[2] Multi-Physical Engineering Sciences Group (MPESG), Aeronautical and Mechanical Engineering Department, School of Science, Engineering and Environment, University of Salford, Manchester M54WT, UK.
[3] Department of Mathematical Sciences, United Arab Emirates University, Al Ain, United Arab Emirates.
[4] Faculty of Engineering, Canadian University Dubai, Dubai, United Arab Emirates.

Abstract. Modern functional nanomaterials coating processes feature an increasing range of intelligent properties including rheology, biological (bio-inspired) modifications, elaborate thermophysical behaviour and complex chemical reactions which are needed for the precise synthesis of bespoke designs. Such manufacturing flow processes are extremely complex and involve both heat and multiple mass transfer (species diffusion) phenomena. Intelligent nano-coatings are particularly attractive since they exploit magnetic nanoparticles which can be manipulated by external magnetic fields. Recently, Boeing Aerospace have explored the use of micro-organisms for intelligent aircraft coatings. Mathematical models provide an excellent analysis for elucidating the response characteristics of such coating dynamics processes. With this motivation, the present analysis is indented to develop a new mathematical model to examine the axisymmetric, magnetohydrodynamic, chemically reactive, gyrotactic bioconvection flow of a tangent hyperbolic nanofluid past a cylinder saturated with Darcy porous medium, as a model of smart-coating enrobing flow. The influence of Cattaneo-Christov heat flux (non-Fourier thermal relaxation parameter), thermophoresis and Brownian motion are taken into consideration. The steady-state, boundary layer, partial differential conservation equations are rendered dimensionless via appropriate transformations and the subsequent nonlinear, coupled, system of governing equations is numerically solved by employing implicit Keller box method. The impact of various factors such as modified Hartmann magnetic number, Weissenberg viscoelastic parameter, Prandtl number, non-Fourier thermal relaxation parameter, thermophoresis, Brownian motion, micro-

organisms concentration difference variable, chemical reaction, bioconvection Peclet number, Schmidt number and bio-convection Schmidt number on the flow, heat transfer, mass transfer, motile density, local friction factor, local heat transfer rate, local mass transfer rate and local microorganism density number wall gradient is visualized graphically. Validation with earlier studies is included. Further validation with a finite element method (FEM) code (SMART-FEM) is presented. Results reveal that the heat transfer upsurges for amplifying the Weissenberg number and Hartmann magnetic number. Microorganism concentration distribution of the non-Newtonian nanofluid coating diminishes for amplifying the bioconvection Schmidt number and Peclet number. Magnifying the power law index parameter reduces the momentum boundary layer thickness of tangent hyberbolic nanofluid while there is an acceleration in the fluid flow near the surface of the cylinder. Nanoparticle Sherwood number rises with higher values of homogenous destructive chemical reaction parameter. The computations provide a solid benchmark for further CFD modelling.

1 Introduction

The continuous demand for functional materials in the 21st century has catalysed significant developments in novel coatings technologies [1] which are increasingly being deployed in a wide range of industries to provide enhanced protection under extreme loading environments. These intelligent or functional materials are highly tunable and synthesized to other size or shape. In addition, these functional materials have the quality to convert energy from one wavelength to another wavelength [2]. An important sub-category of modern smart coating materials are electroactive polymers (EAPs) which combine magnetic particles with polymer melts to create responsive liquids that are easily deposited on engineering components and can be manipulated by external magnetic fields [3]. This permits improved supply chain monitoring and integrity for performance, for example, high temperature corrosive environments. Within this group of EAPs there are also temperature-active magnetic hydrogels and magnetic memory polymers which can sense thermal, mechanical, electric, and magnetic stimuli and respond by changing shape, position, stiffness, and other static and dynamical characteristics. These polymers are rheologically complex and comprise colloidal suspensions of particles form structural chains which can be orientated with respect to the applied magnetic field. Now-a-days, many excellent studies of such functional smart fluids have received much attention. These combine the science of magnetohydrodynamics (MHD) and non-Newtonian fluid dynamics. Butt et al. [4] examined the magnetic field effects on non-Newtonian fluid flow over a stretching surface with slip condition. The two dimensional Non-Newtonian fluid flow through an artery with uniform magnetic field was discussed by Saleem and Munawar [5]. Weidner [6] investigated the dynamics of ferrofluid coatings with the impact of a transverse magnetic field when electric current flows over a horizontal cylinder in the axial direction. The resultant Lorentz force acts on the radial direction and significantly affect the dipoles of the ferrofluid. He interpreted that the surface tension effects cause some variations in thickness of the coating. The magnetic field enforced in the transverse direction improves the coating performance by diminishing the variations in thickness of the coating. In recent years with the advent of nanotechnology, electroactive polymers have been produced which feature embedded nanoparticles and nanostructures (tubes, rods) etc. These provide even further advantages including

* e-mail: sivaraj.kpm@gmail.com

super-hydrophobic properties (to mitigate debris deposition) [7], anti-icing properties [8], etc. Many nanofluids have been invented with enhanced magnetic properties, for example, $Ni - TiN$ hybrid magneto-nanofluids [9], $Co - Fe$ nanocrystals in magnetic polymers [10], $Ni - Mo$ [11], chitosan/sodium phytate/nano-Fe_3O_4 for layered magnetic coatings [12] and magnetic titanium nanostructures [13] which provide enhanced thermal resistance due to the exceptionally high melting point of titanium. In general, various chemical reactions arise during the manufacturing processes of several smart nano-coatings. These are used to engineer specific products with customized properties for different applications e.g. coatings for fuel cells, gas turbine blade surfacing, marine vessel hull finishing etc. Many excellent studies on reactive nano-coating materials have been reported in the literature. For example, Vorobyev et al. [14] analysed the chemical reactions in silver nanoparticles thin film synthesis. He et al. [15] examined the H_2O_2-mediated oxidation of silver nanoparticles. Feng et al. [16] studied the impact of catalytic reactions in platinum-silver nano-hybrid coatings. An excellent appraisal of laboratory methods for chemically reactive nanomaterial synthesis is given by Murr [17]. Further insight into the fabrication of nano-coatings using carbon nanotubes(CNTs) via chemical vapour deposition (CVD) is provided by Kumar and Ando [18]. Commercial procedures are described lucidly by SkySpring Nanomaterials [19], a leading nanocoating company based in Houston, Texas.

To improve on the prediction of the properties and performance of smart magnetic nano-coatings in different applications and furnish a deeper mechanistic appreciation of the actual coating process, mathematical models are indispensable. A popular approach is nanofluid dynamics which emerged from pioneering work conducted at the Argonne Energy Laboratory, Illinois, USA in the mid-1990s directed by Steven Choi. The first book on nanofluids appeared in 2007. This motivated subsequent developments by establishing certain key mechanisms inherent to nanoscale physics such as Brownian motion, thermophoresis, thermal conductivity enhancement mechanisms, ballistic collisions, micro-convection and other phenomena. Subsequently the methodology reported by Das et al. [20] was implemented in many diverse areas of smart coating technology over the past decade or so. These include hydrophobic nanostructured plasma-polymerized intelligent magnetized coatings [21], Nickel-cobalt-silicon carbide electroconductive coatings with enhanced wear properties in manufacturing engineering [22], Nickel-phosphorus and PTFE hybrid magnetic coatings for metallic component surface finishing [23] and titanium-aluminium-vanadium magnetic nanofluid lubricants for surface grinding heat control. Various formulations for simulating nanofluid transport have been developed, notably by Buongiorno [24] at MIT, Koo [25] and Li [26] at North Carolina State University, USA and Tiwari and Das [27] at the Indian Institute of Technology. All these models provide robust approaches for simulating the thermophysical properties of nanofluids, for example, thermal conductivity enhancement of nanofluids. It is to be noted that in addition to momentum and energy conservation equations, Buongiornos model includes the nanoparticle species diffusion equation. Further, this model emphasizes the dominance of thermophoresis body force and Brownian diffusion on nanofluid heat transfer analysis. The Koo and Li models are modifications of the Tiwari-Das volume fraction model. It is to be noted that Tiwari-Das model does not include the nanoparticle species diffusion equation. However, this model permits the analysis of nanoparticle type or shape effects which is not possible in the Buongiorno model. As such the Koo-Li and Tiwari-Das models are more realistic for smart magnetic coating flows where different magnetic nanoparticle species can be studied. Buongiornos model however can compute the distribution of nanoparticle species diffusion in nanofluids. Beg et al. [28] analysed the impact of wall thermal slip on Williamson viscoelastic fluid flow and presented several coating simulations of magnetic nano-polymers. Shukla et al. [29] examined the second law thermodynamic optimization of magnetic nano-coatings.

Non-Newtonian fluids have received more attention during recent decades owing to emerging thermal technologies. The nonlinear rheological behaviour of non-Newtonian fluids are observed in various fluids which are widely used in several industrial and technological applications such as energy storage, oil reservoirs, crystal growth, milk production, pharmaceuticals, fiber technology and intelligent coatings for a variety of engineering systems (naval, aerospace, environmental, biomedical). Many excellent formulations have been developed for rheological fluids which capture different characteristics at different shear rate regimes. The characteristics of various physiological fluids which elucidate the features of non-Newtonian fluids can be exhibited by using the constitutive model of tangent hyperbolic fluid. To list a few, this model robustly describes the characteristics of several biotechnological fluids (cosmetics, facial and body creams for females), paints, blood, respiratory mucus, coatings, and thin film depositions. Experimentally, it has been revealed that the behaviour of shear-thinning phenomenon is simulated more precisely by adopting the tangent hyperbolic fluid model compared with other non-Newtonian fluid models. Shear-thinning behaviour is also known as pseudoplastic behaviour and usually excludes time-dependent effects, such as thixotropy; shear-thinning fluids exhibit a reduction in viscosity with shear strain. Another advantage of the tangent hyperbolic model is, the kinetic molecular theory is utilized to derive the constitutive equations for this model. Recent applications of this model in coating process is received considerable attention. Gaffar et al. [30] examined the hydromagnetic natural convection boundary layer enrobing of a pipe exterior. Malik et al. [31] examined the MHD tangent hyperbolic liquid flow over a stretching cylinder and revealed that the velocity of the fluid significantly declines with an increment in the Weissenberg number and Hartmann number. Ganesh Kumar et al. [32] scrutinized the impact of variable thermal properties on time-dependent squeezing fluid flow towards a sheet by adopting the tangent hyperbolic fluid model. Hayat et al. [33] analysed the influences of MHD, Joule heating and internal wall slip on peristaltic flow in an inclined planar channel by utilizing the tangent hyperbolic nanofluid model. Further studies deploy the tangent hyperbolic model, include, Gaffar et al. [34] (on sphere coating with hydrodynamic and thermal slip), Basha et al. [35] (thermodynamic optimization of magneto-rheological nanofluid from a non-isothermal cylinder), Gaffar et al. [36] (magneto-convection from a perforated inverted cone) and Reddy et al. [37] (Falkner-Skan free and forced convection from a wedge).

Several engineering and industrial applications including thermal coating processes pay much attention to the heat transfer mechanism [38]. Fourier [39] introduced the heat conduction law as the first model for heat transfer in solid bodies. The heat conduction mechanism based on well-known Fouriers law is modified by accounting the finite heat waves to avoid the paradox of thermal relaxation which was finally resolved over a century later by Cattaneo [40]. Christov [41] described the material invariant rule for Maxwell-Cattaneo law by utilizing the Oldroyd upper-convective derivative. The classical Fourier diffusion theory which breaks down in ephemeral problems arise at lowest or highest temperatures can be retrieved as a special case of the Cattaneo-Christov hyperbolic model. The variations in temperature gradient of the heat flux can be adjusted by incorporating a relaxation mechanism in the hyperbolic heat conduction equation derived from the Cattaneo-Christov model. It is to be noticed that within the continuum assumption, the hyperbolic diffusion equation can be obtained by using this model. In recent years, with greater interest in more detailed elaboration of thermal coating processes, many researchers have applied the Cattaneo-Christov heat flux model. Interesting studies of thermal convection using non-Fourier heat flux models were presented by Straughan [42, 43]. Han et al. [44] adopted the non-Fourier thermal relaxation parameter to examine the transport properties of viscoelastic fluid. Mishra et al. [45] used the Adomian decomposition method to study the Von Karman swirling flow between spinning disks with non-

Fourier effects. To scrutinize the heat transfer characteristics of an incompressible fluid, Tibullo and Zampoli [46] derived a unique solution for the heat equation which is modelled based on Cattaneo-Christov model. Mehmood et al. [47] employed the Cattaneo-Christov heat flux model to study the non-orthogonal stagnation flow of a magnetic polymer by adopting the successive linearization method. Numerical investigation to elucidate the characteristics of viscoelastic fluid flow past a stretching surface was studied by Khan et al. [48]. Mishra et al. [49] employed the variational parameter technique to examine the magnetized non-Fourier squeezing lubricant flow between Riga sensor plates with Ohmic dissipation. Further investigations considering non-Fourier thermal conduction, include, Hayat et. al. [50] (on chemically reacting electro-conductive rheological flow) and Elsayed and Beg [51] (ultrasonic heat transfer in biological tissue).

The up-swimming driving movement of micro-organisms is now known to be bioconvection mechanism which opens several fascinating research findings. Bioconvection comprises the propulsion of micro-organisms in peculiar circumstances [52-55]. The motile micro-organisms movement consists of a macroscopic motion and the process is a kind of mesoscale phenomenon. The factors such as combined viscous and gravitational torques (gyrotaxis), oxygen consumption, light (phototaxis), chemical concentration, and magnetic fields may act as a driving force for the upward movement of the micro-organisms. Common micro-organisms include chemotactic bacteria, gyrotactic (bottom-heavy) algae and oxytactic bacteria. Though there are several novel studies have been reported by eminent researchers, Pedley and Kessler [56] lucidly contributed to elucidate the characteristics of bioconvection. It is to be noted that the bioconvection is included as one of the new branches of the biological fluid mechanics. Now-a-days, the researchers significantly concentrate on green technologies and several studies are carried out with an intention to utilize the mechanisms of bioconvection micro-organism in ecologically-oriented engineering systems. In the past two decades several theoretical studies have been reported on bioconvection but there is a lack of engineering interest in this area. In recent days, these mechanisms of propulsion are of great potential use in magnetic functional coatings where micro-organisms can be embedded to achieve very special characteristics such as anti-fouling, hydrophobicity, repulsion of debris, etc. [57-60]. Additionally, motile microorganisms can be added to fluids for particle aggregation prevention. Quite recently, engineers have experimented in combining nanoparticles with motile micro-organisms to achieve dual benefits. Thermal enhancement is produced with nanoparticles and improved mass diffusion and coating homogeneity can be achieved with micro-organisms. These industrial developments have motivated considerable activity in mathematical modelling. Representative studies of nanofluid bioconvection (in which the nanoparticles do not interact with the micro-organisms) include Basir et al. [61] (on transient enrobing coating flow on a stretching cylinder with oxytactic micro-organisms in dilute nanofluid), Siddiqa et al. [62] (on gyrotactic bioconvection nanofluid boundary layer flow from an undulating wall), Zohra et al. [63] (on hydromagnetic oxytactic bioconvection nanofluid swirling flow over a cone with wall transpiration and slip effects), Sudhagar et al. [64] (on axisymmetric free and forced nanofluid bioconvection along an upright cylinder) and Aneja et al. [65] (on microorganism doped magnetic nanofluid coatings for solar collectors). In these studies, it was found among other observations that an augmentation in bioconvection Rayleigh number and bioconvection Lewis number has the tendency to magnify the density of motile microorganisms. In addition, it is found in these investigations that the mechanisms of motile microorganisms and nanoparticles are different since the motion of nanoparticles is caused by the slip mechanisms including thermophoresis and Brownian motion but the motion of motile microorganisms is self-propelled. As a result, the movements of motile microorganisms are independent of the movements of

nanoparticles. It is noticed that the critical Rayleigh numbers may either depress or elevate due to the nanoparticles while a constant destabilization impact is observed in case of micro-organisms. Thermophilic microorganisms, for example, Bacillus thermo glucosidasius and Bacillus licheniformis in particular, are relevant to nano-coatings and are currently being explored.

Inspection of the literature has shown that so far no study exists on analysing the magnetohydrodynamic tangent hyperbolic nanofluid flow along a vertical cylinder saturated with Cattaneo-Christov heat flux, Darcian porous medium, and chemical reaction impacts with gyrotactic micro-organisms. Therefore, the present analysis focuses on this study. Buongiornos two-component dilute nanoscale model is considered with thermophoresis and Brownian motion features. The tangent hyperbolic model is implemented for nanofluid rheology. The steady-state partial differential governing equations are converted into a non-dimensional system of nonlinear, coupled, two-parameter system of differential equations with associated wall and free stream conditions which are solved by adopting the implicit Keller box method. Verification of computations is achieved with a variational finite element method code (SMART-FEM) and a special case from the literature. The impact of the key emergent parameters i.e. modified Hartmann magnetic number, Weissenberg viscoelastic parameter, non-Fourier thermal relaxation parameter, Schmidt number, thermophoresis, Brownian motion, Prandtl number, chemical reaction, micro-organisms concentration difference variable, bioconvection Peclet number and bio-convection Schmidt number on fluid velocity, heat transfer, concentration, motile micro-organism density number, local friction factor, local heat transfer rate, local mass transfer rate and local microorganism density number wall gradient is visualized graphically.

2 Bioconvection-nanofluid smart coating model

In the coating model developed, the two-dimensional, steady, incompressible, laminar flow of an electrically-conducting tangent hyperbolic nanofluid past a vertical cylinder of radius, a, doped with micro-organisms immersed in a Darcian porous medium in an (x, y) co-ordinate system is considered. This requires a combined nanofluid bioconvection formulation. The suspension of the nanoparticle is considered to be stable which results in the absence of nanoparticle agglomeration. It is to be noted that the swimming direction and the swimming velocity of gyrotactic microorganisms are not affected due to the presence of nanoparticles when the concentration of the suspended nanoparticles is less than 1%. Further, the impact of bioconvection is incited when the concentration of the suspended nanoparticles is low. The influence of bioconvection is suppressed when the concentration of the suspended nanoparticles is high. The present analysis is modelled based on the Oberbeck-Boussinesq approximation which is valid for the dilute nanoparticle concentrations. Based on these assumptions, the conservation equations [63] can be written in generalized vectorial form as follows:
Continuity (mass conservation) equation:

$$\nabla.\bar{V} = 0 \tag{1}$$

Momentum equation:

$$\frac{\mu}{K}\bar{V} = -\nabla p + \left[C\rho_p + (1-C)\left\{\rho_f\left(1-\beta_2\left(T-T_\infty\right)\right)\right\} + N^*\gamma\Delta\rho\right]g_a \tag{2}$$

Energy equation:

$$\bar{V}.\nabla T = \alpha_m\nabla^2 T + \tau\left[D_B\nabla C.\nabla T + \left({}^{D_T}/_{T_\infty}\right)\nabla T.\nabla T\right] \tag{3}$$

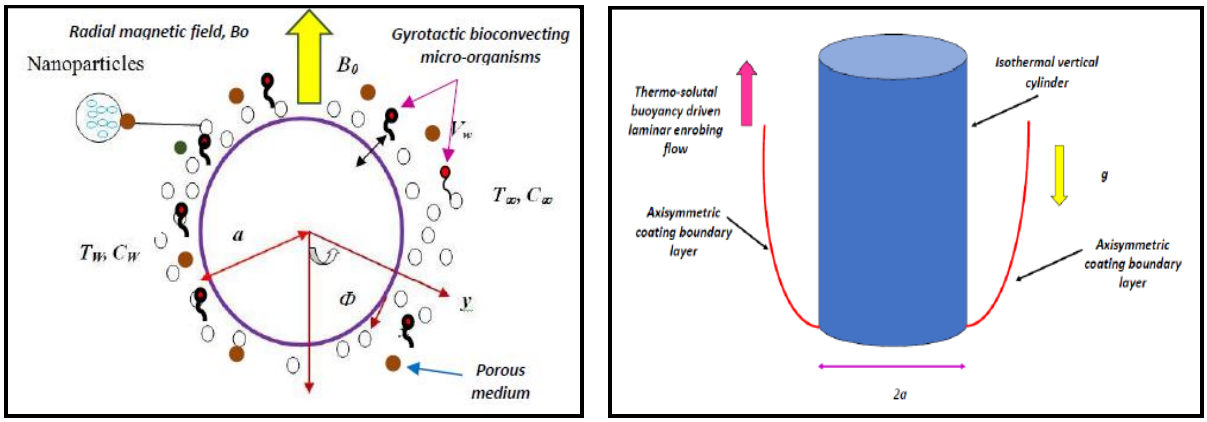

(a) (b)

Fig. 1. Magnetohydrodynamic gyrotactic bioconvection nanofluid smart coating flow on cylinder- a) end elevation b) front elevation

Nanoparticle conservation equation:

$$\bar{V}.\nabla C = D_B \nabla^2 C + \left[\left(D_T/T_\infty\right)\nabla^2 T\right] \tag{4}$$

Microorganisms equation:

$$\nabla . j = 0 \tag{5}$$

The microorganisms flux, j, is considered as:

$$j = N^* \bar{V} + N^* V^* - D_n N^* \tag{6}$$

The following linearized momentum equation is attained from Eqn. (2) with an appropriate selection for the reference pressure.

$$-\frac{\mu}{K}\bar{V} = -\nabla p + \left[\left(\rho_p - \rho_{f\infty}\right)\left(C - C_\infty\right) + \beta_2\left(1 - C_\infty\right)\rho_{f\infty}\left(T - T_\infty\right) + N^*\gamma\Delta\rho\right] g_n \tag{7}$$

V^* is simplified as follows:

$$V^*\left(\bar{u}, \bar{v}\right) = \left(bW_c/\Delta C\right)\nabla C \tag{8}$$

Here $\bar{u} = \left(bW_c/\Delta C\right)\left(\partial C/\partial x\right)$ and $\bar{v} = \left(bW_c/\Delta C\right)\left(\partial C/\partial y\right)$. where, b is the chemotaxis constant, W_c is the maximum cell swimming speed $\bar{V}$ is the nanofluid velocity, V^* is the average directional swimming velocity of a microorganism, T is the temperature C is the nanoparticle concentration, p is the pressure, N^* is the density of motile microorganisms, g_n is the gravity vector, ∇^2 is the Laplacian operator, D_n is the diffusivity of microorganisms (Hill-Kessler-Pedley model), K is permeability of the homogenous, isotropic, saturated porous medium, β_2 is the volumetric volume expansion coefficient of the nanofluid, ρ_p is the density of the particles, ρ_f is the fluid density, μ is the fluid viscosity, γ is the average volume of a microorganism, D_B is the Brownian diffusion coefficient (Buongiorno nanoscale model), D_T is the thermophoretic diffusion coefficient (Buongiorno nanoscale model). The buoyancy term

due to up swimming of microorganisms in the momentum Eqn. (2) and conservation equation for microorganisms (5) is popularly used. The Eqns. (1) - (5) can be further extended by incorporating a magnetic body force term, hyperbolic tangent rheological model and non-Fourier (Cattaneo-Christov heat flux) thermophysics. A uniform strength of magnetic field B_0 is applied normal to the cylinder as shown in Fig 1. T_w and T_∞ are the cylindrical surface temperature and ambient fluid temperature ($T_w > T_\infty$). C_w and C_∞ are the concentration and ambient concentration ($C_w > C_\infty$). N_w^* and N_∞^* are density of surface concentration of microorganisms and ambient concentration of microorganisms. Under the boundary-layer approximation, in Cartesian coordinates, the governing equations for steady MHD tangent hyperbolic nanofluid bioconvection coating flow with magnetic drag (Lorentz) emerge as:

$$\frac{\partial u}{\partial x}+\frac{\partial v}{\partial y}=0, \tag{9}$$

$$\begin{aligned} u\tfrac{\partial u}{\partial x}+v\tfrac{\partial u}{\partial y} &= \nu_f\left(1-n_1\right)\tfrac{\partial^2 u}{\partial y^2}+\sqrt{2}\nu_f n_1\Gamma\tfrac{\partial u}{\partial y}\tfrac{\partial^2 u}{\partial y^2}-\left(\tfrac{\sigma_f B_0^2}{\rho_f}+\tfrac{\nu_f}{K}\right)u \\ &\quad +g_a\begin{bmatrix}\beta_2(1-C_\infty)(T-T_\infty)-\frac{1}{\rho_f}(\rho_p-\rho_f)(C-C_\infty)\\ -\frac{1}{\rho_f}(\rho_m-\rho_f)\gamma(N^*-N_\infty^*)\end{bmatrix}\sin\left(\tfrac{x}{a}\right), \end{aligned} \tag{10}$$

$$\begin{aligned} u\tfrac{\partial T}{\partial x}+v\tfrac{\partial T}{\partial y} &= \tfrac{k_f}{(\rho c_p)_f}\tfrac{\partial^2 T}{\partial y^2}+\tau\left[D_B\tfrac{\partial C}{\partial y}\tfrac{\partial T}{\partial y}+\tfrac{D_T}{T_\infty}\left(\tfrac{\partial T}{\partial y}\right)^2\right] \\ &\quad -\gamma_1\begin{pmatrix}\left(u\frac{\partial u}{\partial x}+v\frac{\partial u}{\partial y}\right)\frac{\partial T}{\partial x}+\left(u\frac{\partial v}{\partial x}+v\frac{\partial v}{\partial y}\right)\frac{\partial T}{\partial y}\\ +2uv\frac{\partial^2 T}{\partial x\partial y}+u^2\frac{\partial^2 T}{\partial x^2}+v^2\frac{\partial^2 T}{\partial y^2}\end{pmatrix}, \end{aligned} \tag{11}$$

$$u\frac{\partial C}{\partial x}+v\frac{\partial C}{\partial y}=D_B\frac{\partial^2 C}{\partial y^2}+\frac{D_T}{T_\infty}\frac{\partial^2 T}{\partial y^2}-K_c\left(C-C_\infty\right), \tag{12}$$

$$u\frac{\partial N^*}{\partial x}+v\frac{\partial N^*}{\partial y}=D_n\frac{\partial^2 N^*}{\partial y^2}-\frac{bW_c}{C_\infty}\left[\frac{\partial}{\partial y}N^*\left(\frac{\partial C}{\partial y}\right)\right], \tag{13}$$

The boundary restrictions are:

$$\begin{aligned} &y=0: u=0, v=V_w,\ T=T_w,\ \ C=C_w,\ \ N^*=N_w^* \\ &y\to\infty: u\to 0,\ T\to T_\infty,\ \ C\to C_\infty,\ \ N^*\to N_\infty^*. \end{aligned} \tag{14}$$

The equation of continuity is satisfied by choosing the stream function ψ as $u=\partial\psi/\partial y$ and $v=-\partial\psi/\partial x$. The non-dimensional variables are considered as follows:

$$\begin{aligned} &\xi=\frac{x}{a},\qquad \eta=\frac{y}{a}\sqrt[4]{Gr},\qquad f(\xi,\eta)=\frac{\psi}{\nu_f\xi\sqrt[4]{Gr}}, \\ &\theta(\xi,\eta)=\frac{T-T_\infty}{T_w-T_\infty},\qquad \phi(\xi,\eta)=\frac{C-C_\infty}{C_w-C_\infty},\qquad \Psi(\xi,\eta)=\frac{N^*-N_\infty^*}{N_w^*-N_\infty^*}. \end{aligned} \tag{15}$$

Based on Eqn. (15), Eqn. (9) is eliminated and Eqns. (10)-(13) become:
Momentum boundary layer equation:

$$\begin{aligned} &\left(1-n_1\right)f'''+n_1We f''f'''+ff''-f'^2-\left(\tfrac{1}{D_a}+Ha\right)f' \\ &\qquad +\left(\theta-N\phi-Rb\Psi\right)\tfrac{\sin\xi}{\xi}=\xi\left[\tfrac{\partial f'}{\partial\xi}f'-\tfrac{\partial f}{\partial\xi}f''\right] \end{aligned} \tag{16}$$

Energy (thermal) boundary layer equation:

$$\frac{\theta''}{P_r}+N_b\phi'\theta'+N_t\theta'^2+f\theta'-\gamma_1^*\left(ff'\theta'+f^2\theta''\right)=\xi\left\{\begin{array}{l}\frac{\partial\theta}{\partial\xi}\left[\gamma_1^*\left(f'^2-ff''\right)+f'\right]\\-\frac{\partial f}{\partial\xi}\left[\theta'\left(\gamma_1^*f'+1\right)\right]\\+\gamma_1^*f\left[\frac{\partial f'}{\partial\xi}\theta'-2\frac{\partial\theta'}{\partial\xi}f'\right]\end{array}\right\} \quad (17)$$

Nanoparticle species boundary layer equation:

$$\frac{1}{Sc}\phi''+\frac{N_t}{ScN_b}\theta''-Kr\phi+f\phi'=\xi\left[\frac{\partial\phi}{\partial\xi}f'-\frac{\partial f}{\partial\xi}\phi'\right] \quad (18)$$

Microorganism species boundary layer equation:

$$\frac{1}{Sb}\Psi''-\frac{Pe}{Sb}\left[\phi''\left(N_m+\Psi\right)+\phi'\Psi'\right]+f\Psi'=\xi\left[\frac{\partial\Psi}{\partial\xi}f'-\frac{\partial f}{\partial\xi}\Psi'\right], \quad (19)$$

The corresponding non-dimensional boundary conditions are:

$$\begin{aligned}&\eta=0: f'=0,\ f=f_w,\theta=1,\phi=1,\Psi=1.\\&\eta\to\infty: f'\to0,\theta\to0,\phi\to0,\Psi\to0.\end{aligned} \quad (20)$$

In the above equations, Φ is the azimuthal coordinate, ξ is the dimensionless tangential coordinate and the primes denote differentiation with respect to the dimensionless radial coordinate η. $We\left(=\frac{\sqrt{2}\nu_f\Gamma_x Gr^{\frac{1}{4}}}{a^2}\right)$ is the Weissenberg number (ratio of elastic forces to the viscous forces and also the relation of stress relaxation time of the fluid to a specific process time), $P_r\left(=\frac{\rho_f\nu_f c_p}{k_f}\right)$ is the Prandtl number, $Da\left(=\frac{K\sqrt{Gr}}{a^2}\right)$ is a Darcy parameter (dimensionless scaled permeability), $N_t\left(=\tau\frac{D_T(T_w-T_\infty)}{\nu_f}\right)$ is the Buongiorno thermophoretic body force parameter, $N_b\left(=\tau\frac{D_B(C_w-C_\infty)}{\nu_f}\right)$ is the Buongiorno Brownian motion parameter, $Sc\left(=\frac{\nu_f}{D_B}\right)$ is the Schmidt number (ratio of momentum and nanoparticle species diffusion rate), $N\left(=\frac{(\rho_p-\rho_f)(C_w-C_\infty)}{(1-C_\infty)\rho_f\beta_2(T_w-T_\infty)}\right)$ is the buoyancy ratio parameter (ratio of thermal and solutal i.e. species buoyancy forces), $Rb\left(=\frac{(\rho_m-\rho_f)\gamma(N_w^*-N_\infty^*)}{(1-C_\infty)\rho_f\beta_2(T_w-T_\infty)}\right)$ is the bioconvection Rayleigh number, $f_w\left(=\frac{-V_w a}{\nu_f\sqrt{Gr}}\right)$ is the blowing/suction parameter (cylinder surface transpiration parameter; $f_w>0$ for $V_w>0$ (the case of blowing), and $f_w>0$ for $V_w<0$ (the case of suction) and $f_w=0$ for a solid impervious cylinder), $\gamma_1^*\left(=\frac{\gamma_1\nu_f Gr^{1/2}}{a^2}\right)$ thermal relaxation parameter (Cattaneo-Christov non-Fourier hyperbolic parameter; when $\gamma_1^*\to0$, the classical Fourier model is retrieved), $Ha\left(=\frac{\sigma_f B_0^2 a^2}{\rho_f\nu_f\sqrt{Gr}}\right)$ is the modified Hartmann magnetic parameter, $Gr\left(=\frac{g_a\beta_2(T_w-T_\infty)a^3}{\nu_f^2}\right)$ is the Grashof number (free convection parameter i.e. ratio of thermal buoyancy to viscous hydrodynamic forces), $Pe\left(=\frac{bW_c}{\nu_f}\right)$ is the bioconvection Peclet number , $Sb\left(=\frac{\nu_f}{D_n}\right)$ is the bioconvection Schmidt number (ratio of the momentum diffusion rate to the micro-organism species diffusion rate) and $N_m\left(=\frac{N^*}{N_w^*-N_\infty^*}\right)$ is the micro-organism concentration difference variable. Important design quantities in manufacturing coating fluid dynamics are the skin-friction

coefficient, heat transfer rate, mass transfer rate and density number of motile microorganism at the surface of the cylinder. These are defined respectively as:

$$Cf_x Gr^{-3/4} = (1-n_1)\,\xi f''(\xi,0) + \frac{n_1}{2} We\,\xi\,(f''(\xi,0))^2\,, \tag{21}$$

$$Nu_x Gr^{-1/4} = -\theta'(0)\,, \tag{22}$$

$$Sh_x Gr^{-1/4} = -\phi'(0)\,, \tag{23}$$

$$Nh_x Gr^{-1/4} = -\Psi'(0) \tag{24}$$

3 Solution procedure of Keller box method (KBM)

The dimensionless nonlinear, coupled, partial differential equations as defined by Eqns. (16)-(19) with transformed conditions (20) are solved numerically using the unconditionally stable second-order accurate KBM. This technique is ideal for nonlinear parabolic differential equation systems and therefore an excellent choice to examine the characteristics of laminar boundary layer coating dynamics. The solution procedure of KBM is given below:

- The first order differential equations are obtained from the higher order differential equations by introducing transformation variables.
- A central difference grid approximation scheme is utilized to discretize the resultant first order differential equations.
- Newton's method is employed to linearize the algebraic equations.
- The block tri-diagonal elimination system is acquired to solve the resultant block matrix system.

Table 1. A grid independence study for local Nusselt number

Step size	Nu_x		
$\Delta\eta$	$\eta_\infty = 9$	$\eta_\infty = 12$	$\eta_\infty = 14$
0.5	0.4259	0.4260	0.4260
0.1	0.4200	0.4201	0.4201
0.05	0.4198	0.4199	0.4199
0.01	0.4198	0.4199	0.4199

In the present problem, the streamwise coordinate (ξ) and radial (transverse) coordinate (η) ranges are considered as 1 and 9, respectively, following a convergence study. A grid independence study for local Nusselt number with different grid sizes in the radial direction $\Delta\eta$ is elucidated in Table 1. The solution of this analysis is obtained by fixing the increment in the radial direction as 0.05 (i.e. $\Delta\eta = 0.05$) and a $20X180$ mesh (grid) is designed for the boundary layer domain. In the present analysis, the convergence criteria is determined as 0.00001 at all grid points.

4 Validation of numerical scheme

A comparison analysis is executed to examine the accuracy of the KBM solutions and the results are documented in Table 2. The comparison results reveal that the local rate of heat transfer for various values of (ξ) closely matches with the results of Merkin [66], Gaffar et al. [30] and Nazar et al. [67].

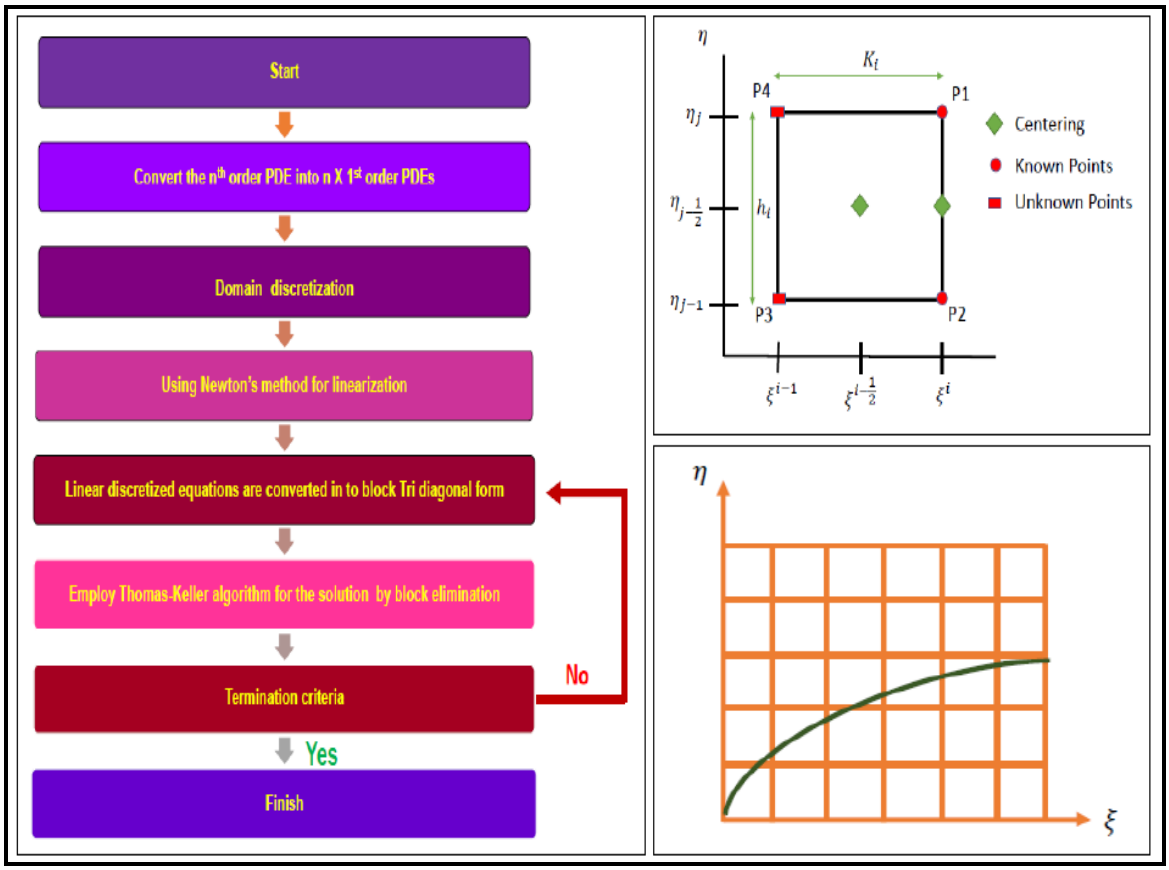

Fig. 2. Numerical methodology- Keller box algorithm flow chart, Keller box scheme and boundary layer mesh

Table 2. Comparison of current results with Merkin [66], Gaffar et al. [30], Nazar et al. [67] for local Nusselt number with various values of ξ when $N_t = N_b = \gamma_1^* = Ha = We = n_1 = N = Rb = Pe = Sc = Sb = N_m = Kr = 0, Sc = 0.6,\ Ha = 0.5,\ P_r = 7$.

ξ	Nu_x				
	Merkin [66]	Gaffar et al. [30]	Nazar et al [67]	KBM	FEM
0^0 (lower stagnation point)	0.4214	0.4213	0.4214	0.4124	0.4123
$\frac{\pi}{6}$	0.4161	0.4160	0.4161	0.4162	0.4161
$\frac{\pi}{4}$	0.4007	0.4005	0.4004	0.4005	0.4006
$\frac{\pi}{2}$	0.0375	0.3742	0.3741	0.3744	0.3743
π (upper stagnation point)	0.1945	0.1917	0.1916	0.1922	0.1919

5 Further validation with variational FEM code SMART-FEM

Benchmarking with previous studies only afford limited verification of solutions. For example in Table 1, no less than 12 parameters have to be set to zero to validate

with much simpler earlier studies i.e. when $N_t = N_b = \gamma_1^* = Ha = We = n_1 = N = Rb = Pe = Sc = Sb = N_m = Kr = 0, Sc = 0.6, Ha = 0.5, P_r = 7$. The solutions in Table 1 therefore neglect all nanoscale, bioconvection, mass transfer, non-Newtonian and chemical reaction effects. To validate the full KBM solution of the general model, an alternative numerical code must be employed. The robust variational finite element method (FEM) [68] is therefore deployed. This approach is the most popular in engineering sciences and has been extensively employed in many complex multifunctional materials fluid dynamics simulations- see [69-74], all of which feature the in-house MATLAB-based program, SMART-FEM. It is to be noted that the SMART-FEM code is equally efficient for solving the ordinary differential equations and partial differential equations with initial conditions as well as boundary conditions. Since the boundary value problem is of two-parameter type, quadrilateral finite elements are required. The formulation is briefly described as follows:

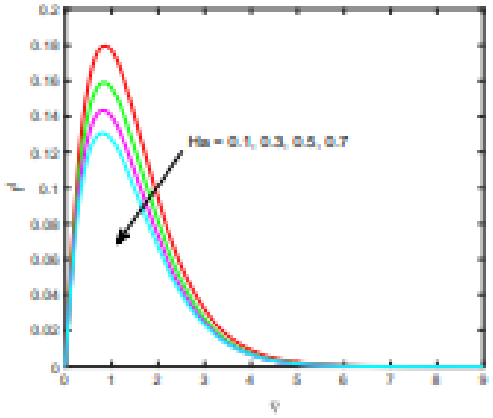

Fig. 3. Plot of f' with various Hartmann numbers.

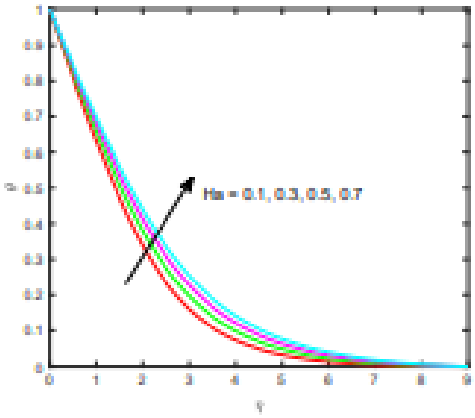

Fig. 4. Plot of θ with various Hartmann numbers.

Variational formulation:

The variational form associated with Eqns. (16) - (19) over a typical quadrilateral

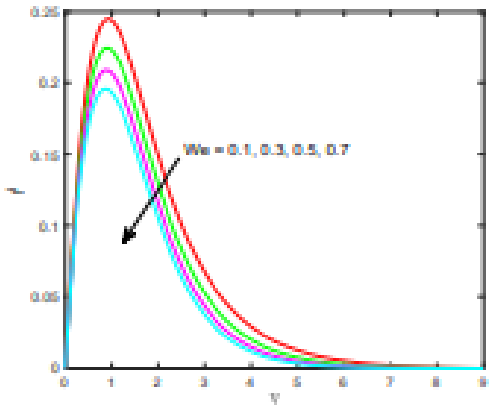

Fig. 5. Plot of f' with different Weissenberg numbers.

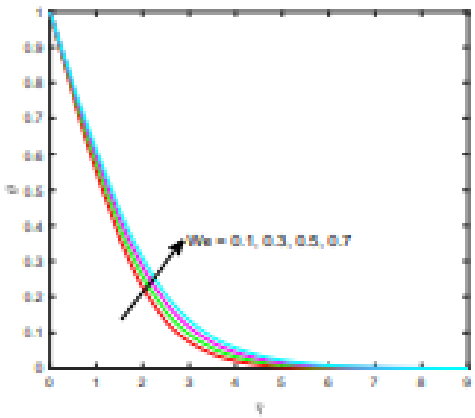

Fig. 6. Plot of θ with various Weissenberg numbers

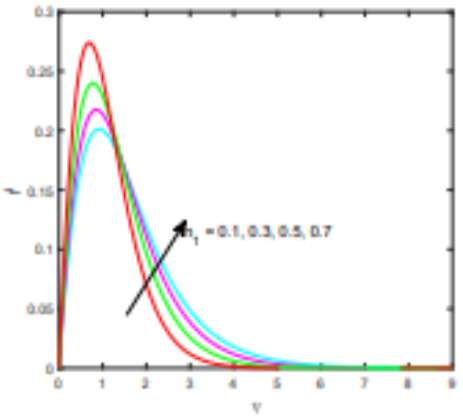

Fig. 7. Plot of f' for various tangent-hyperbolic power-law index parameters

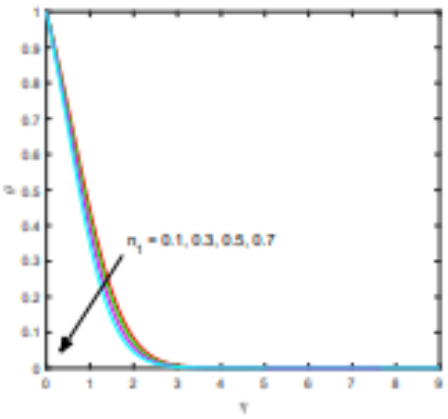

Fig. 8. Plot of θ for enhancing tangent-hyperbolic power-law index parameters.

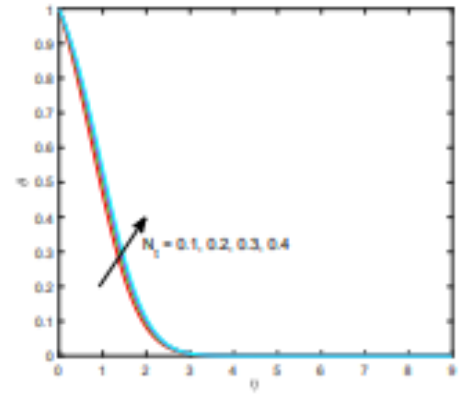

Fig. 9. Plot of θ for various thermophoretic parameter.

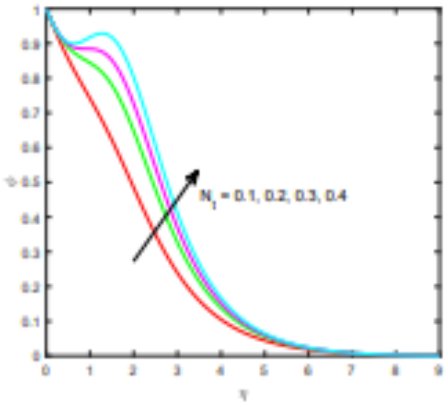

Fig. 10. Plot of ϕ for various thermophoretic parameter.

element in the (ξ, η) coating boundary layer domain is given by:
Momentum

$$\int_{\Omega^e} W_1 \left(\begin{array}{l} (1-n_1) f''' + n_1 We f'' f''' + f f'' - \left(\frac{1}{Da} + Ha\right) f' \\ -f'^2 + (\theta - N\phi - Rb\wp) \frac{\sin\xi}{\xi} - \xi \left[\frac{\partial f'}{\partial \xi} f' - \frac{\partial f}{\partial \xi} f'' \right] \end{array} \right) \partial\xi \partial\eta = 0, \quad (25)$$

Energy

$$\int_{\Omega^e} W_2 \left(\begin{array}{l} \frac{\theta''}{P_r} + N_b \phi' \theta' + N_t \theta'^2 + f\theta' \\ -\gamma_1^* \left(f f' \theta' + f^2 \theta'' \right) - \\ \xi \left\{ \begin{array}{l} \frac{\partial \theta}{\partial \xi} \left[\gamma_1^* \left(f'^2 - f f'' \right) + f' \right] \\ -\frac{\partial f}{\partial \xi} \left[\theta' \left(\gamma_1^* f' + 1 \right) \right] \\ +\gamma_1^* f \left[\frac{\partial f'}{\partial \xi} \theta' - 2 \frac{\partial \theta'}{\partial \xi} f' \right] \end{array} \right\} \end{array} \right) \partial\xi \partial\eta = 0, \quad (26)$$

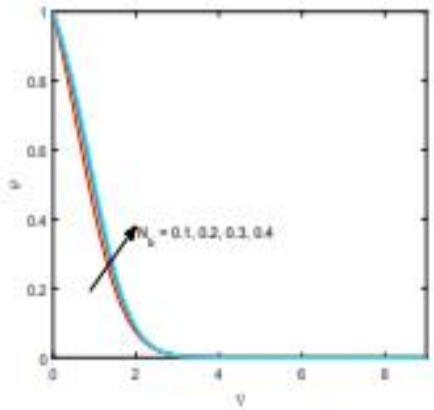

Fig. 11. Plot of θ for different Brownian motion parameter.

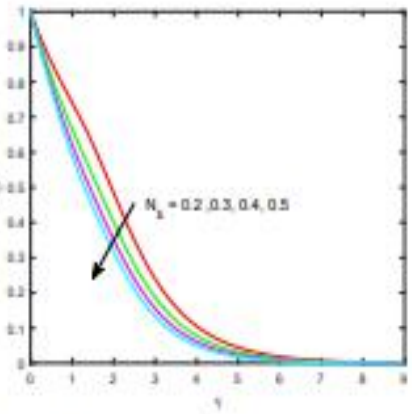

Fig. 12. Plot of ϕ for different Brownian motion parameter.

Nano-particle species diffusion

$$\int_{\Omega^e} W_3 \left(\begin{array}{c} \frac{1}{Sc}\phi'' + \frac{N_t}{ScN_b}\theta'' - Kr\phi + f\phi' \\ -\xi\left[\frac{\partial\phi}{\partial\xi}f' - \frac{\partial f}{\partial\xi}\phi'\right] \end{array} \right) \partial\xi\partial\eta = 0, \tag{27}$$

Gyrotactic micro-organism number density

$$\int_{\Omega^e} W_4 \left(\begin{array}{c} \frac{1}{Sb}\Psi'' - \frac{P_E}{Sb}\left[\phi''\left(N_m + \Psi\right) + \phi'\Psi'\right] + f\Psi' \\ -\xi\left[\frac{\partial\Psi}{\partial\xi}f' - \frac{\partial f}{\partial\xi}\Psi'\right] \end{array} \right) \partial\xi\partial\eta = 0, \tag{28}$$

The arbitrary test functions W_1, W_2, W_3 and W_4 are introduced in order to elucidate the changes in f, θ, ϕ and Ψ. These functions are considered as primary variables since examining the boundary term in the above equations elucidates that the specification of the function constitutes the necessary boundary condition. The specification of the coefficient of the weight functions in the boundary expression constitutes the natural boundary condition, although secondary variables of the formulation are embedded with in the conditions.

Shape Functions:
Quadrilateral elements are selected which approximate the boundary layer region (similar to the rectangular Keller box cells used earlier) well. With an aspect ratio of unity, the converge of square elements with linear interpolation functions are faster compared with rectangular or triangular elements. Further details about the description of elements can be found in Reddy [68]. It is to be noted that ψ_1, ψ_2, ψ_3, and ψ_4 are considered as linear interpolation functions for a square element Ω^e which are excluded here for brevity.

Finite Element Formulation: The structure domain defined as: $0 \leq \xi \leq 1$ and $0 \leq \eta \leq 1$ is discretized into square elements of the same size with the finite element approximations:

$$\begin{aligned} f &= \sum\nolimits_{j=1}^{n} f_j\psi_j\left(\xi,\eta\right), \theta = \sum\nolimits_{j=1}^{n} \theta_j\psi_j\left(\xi,\eta\right), \\ \phi &= \sum\nolimits_{j=1}^{n} \phi_j\psi_j\left(\xi,\eta\right), \Psi = \sum\nolimits_{j=1}^{n} \Psi_j\psi_j\left(\xi,\eta\right), \end{aligned} \tag{29}$$

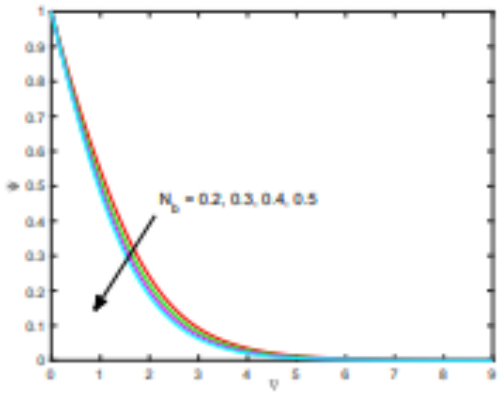

Fig. 13. Plot of Ψ for different Brownian motion parameter.

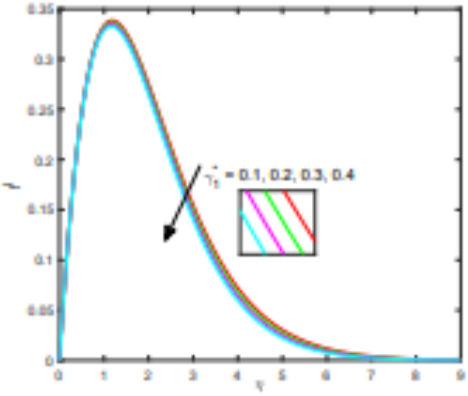

Fig. 14. Plot of f' for various non-Fourier (thermal relaxation) parameter.

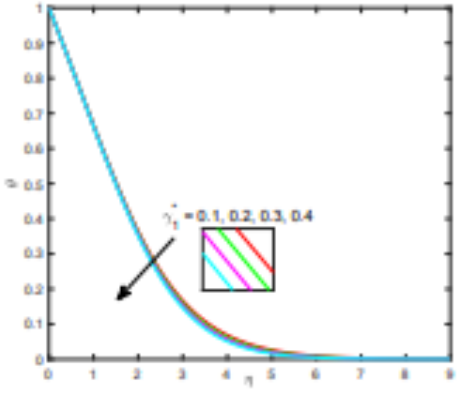

Fig. 15. Plot of θ for various non-Fourier (thermal relaxation) parameter.

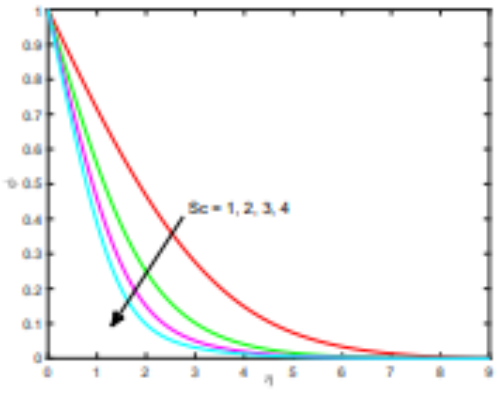

Fig. 16. Plot of ϕ for various Schmidt numbers.

Here n=3, 4, 6 and 8, in order, corresponds to a linear triangular element, linear rectangular element, quadratic triangular element and quadratic rectangular element. Effectively, for the finite element model of the problem at hand, the following matrix-vector system emerges:

$$\left[K^{11}\right] = \begin{bmatrix} K_{11}^{11} & K_{12}^{11} & K_{13}^{11} & K_{14}^{11} \\ K_{21}^{11} & K_{22}^{11} & K_{23}^{11} & K_{24}^{11} \\ K_{31}^{11} & K_{32}^{11} & K_{33}^{11} & K_{34}^{11} \\ K_{41}^{11} & K_{42}^{11} & K_{43}^{11} & K_{44}^{11} \end{bmatrix}, \{f_\xi\} = \begin{Bmatrix} f_{\xi 1} \\ f_{\xi 2} \\ f_{\xi 3} \\ f_{\xi 4} \end{Bmatrix},$$

$$and \left\{r^1\right\} = \begin{Bmatrix} r_1^1 \\ r_2^1 \\ r_3^1 \\ r_4^1 \end{Bmatrix}, \qquad (30)$$

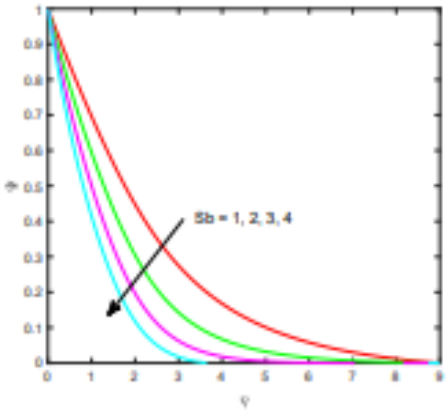

Fig. 17. Plot of Ψ for bioconvection Schmidt numbers.

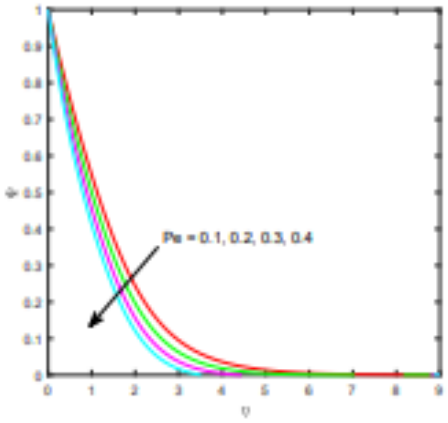

Fig. 18. Plot of Ψ with various bioconvection Peclet numbers.

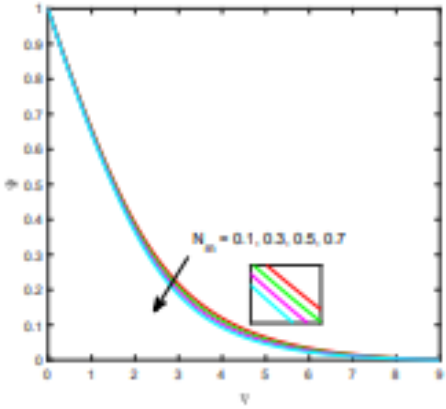

Fig. 19. Plot of Ψ with micro-organism concentration difference parameter.

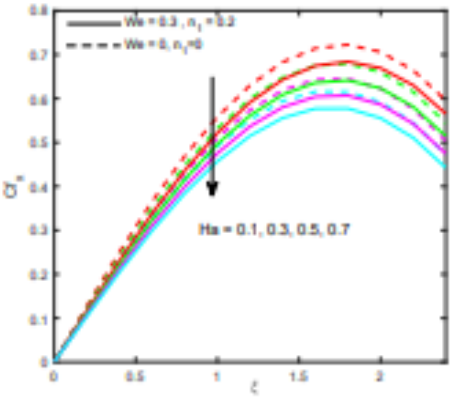

Fig. 20. Skin friction distribution with various Hartmann magnetic numbers, Weissenberg numbers and tangent-hyperbolic power-law index parameter values.

where

$$\overline{f_\xi} = \sum_{i=1}^{4} \psi_i f_{\xi_i}, \qquad \overline{f_\eta} = \sum_{i=1}^{4} \psi_i f_{\eta_i} \tag{31}$$

The entire domain is separated into 100 square elements of length 0.1. Every element is four-noded, therefore, entire domain comprises 121 nodes. Four functions need to be evaluated at every node. Therefore a system of 484 equations is obtained after introducing the element equations. The resultant nonlinear equations are solved by adopting a suitable iterative scheme. By introducing the suitable known functions, the system is linearized. The well-known Gausss elimination method is utilized to solve the system of linear equations with an accuracy of 5×10^{-4}. It is important to note that the accuracy is not affected for increasing the number of elements by reducing the size of the elements in the same domain. This indicates that mesh independence is achieved. The comparison of FEM and KBM is shown in Table 3 with all parameter

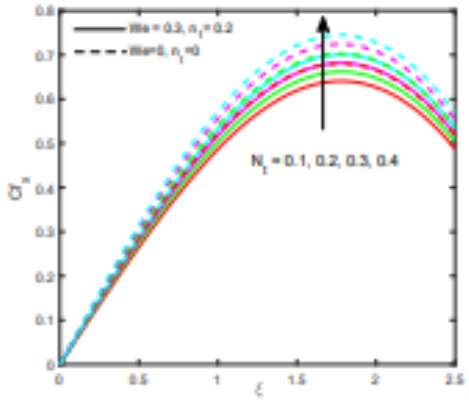

Fig. 21. Skin friction profiles with various thermophoretic nanoscale numbers, Weissenberg numbers and tangent-hyperbolic power-law index parameter values.

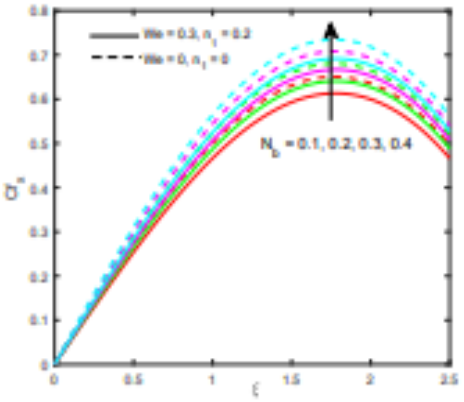

Fig. 22. Skin friction evolution with various Brownian motion nanoscale numbers, Weissenberg numbers and tangent-hyperbolic power-law index parameter values.

values set at $Ha = 0.5$, $N = 0.1$, $Rb = 0.1$, $Da = 1.0$, $\gamma_1^* = 0.1$, $N_b = 0.3$, $N_t = 0.1$, $We = 0.3$, $Pe = 0.1$, $Sc = 0.6$, $Sb = 1$, $N_m = 0.1$, $Kr = 0.3$, $P_r = 7$ unless otherwise specified. The comparison results reveal that a good agreement is attained among the results obtained by adopting the KBM code and FEM code.

6 Results and discussion

This section examines the influence of all key parameters i.e. Hartmann magnetic parameter, Weissenberg number, Brownian motion parameter, thermophoresis parameter, Darcy parameter, Schmidt number, chemical reaction parameter, bioconvection Schmidt number, bioconvection Peclet number and micro-organism concentration difference variable on fluid flow, heat transfer, nanoparticle concentration and motile micro-organism density number and presented the results through graphs and tables. The pertinent parameters of the present computation are fastened with the following values: $Ha = 0.5$, $N = 0.1$, $Rb = 0.1$, $Da = 1.0$, $\gamma_1^* = 0.1$, $N_t = 0.1$, $N_b = 0.3$, $Kr = 0.3$, $Sc = 0.6$, $Pe = 0.1$, $Sb = 1$, $We = 0.3$, $N_m = 0.1$, and $P_r = 7$. This data corresponds to actual functional magnetic nanofluid coatings see [20], [38] and [75]. The impact of magnetic field parameter i.e. Hartmann number (Ha) on flow and temperature distributions, in order, are illustrated in Figs. 3 and 4. The results reveal that an enhance in the magnetic parameter decelerates the fluid flow. However, the opposite trend is observed in temperature profiles i.e. the heat transfer is strongly boosted with stronger magnetic field. Physically, the drag force (Lorentz force) retards the fluid velocity along the surface of cylinder. It impedes the flow which enables enhanced control of the coating regime. However, the temperature is magnified along the surface of cylinder because of the dissipated heat due to the auxiliary effort consumed in dragging the fluid against the applied magnetic field. A transverse retarding body force is generated due to the magnetic field applied in the radial axis of the cylindrical surface. This declines the fluid flow and weakens the velocity boundary layer thickness. It is an evidence that the magnetic field applied in the radial axis significantly controls the momentum development in the coating region. As observed from the figure, the impact of the magnetic field is prominent near the surface of cylinder. On the other hand, the thermal boundary layer thickness is amplified since

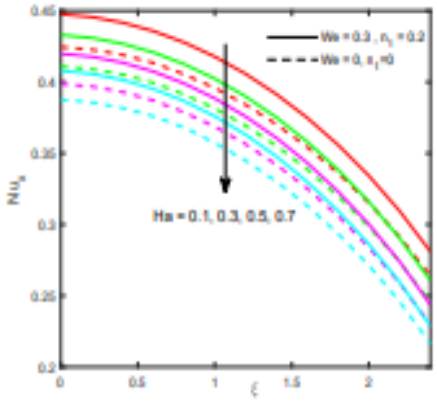

Fig. 23. Heat transfer rate profiles with various magnetic Hartmann numbers, Weissenberg numbers and tangent-hyperbolic power-law index parameter values.

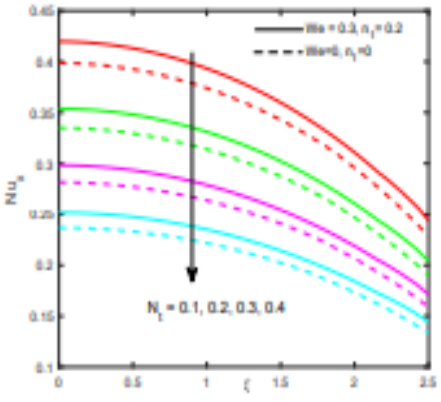

Fig. 24. Heat transfer rate profiles with various thermphoretic nanoscale numbers, Weissenberg numbers and tangent-hyperbolic power-law index parameter values.

the coating regime is energized in the boundary layer. The impact of the magnetic field is significant in the middle of the thermal boundary layer. From the literature, it is noticed that the heat transfer investigations on MHD non-Newtonian coating flows elucidate the similar momentum and thermal boundary layer characteristics. In both figures and indeed in all other plots versus radial coordinate, asymptotically smooth convergence is achieved at outer edge of the boundary layer coating (the free stream) which confirms the suitability of the KBM finite difference code for adopting the large values for infinity boundary condition.

Figures 5 and 6 indicate that elevation in Weissenberg number strongly depletes the velocity whereas it elevates the fluid temperature i.e. it exerts a similar role to magnetic field by retarding the axisymmetric boundary layer axial flow and heating the coating. The ratio of elastic forces to viscous forces is known as Weissenberg number (We). The characteristics of Newtonian fluid is observed when the value of the Weissenberg number tends to zero and the characteristics of elastic solid is observed when the value of the Weissenberg number tends to infinity. The characteristic of magnetic polymeric viscoelastic fluid is observed for the other value of Weissenberg number. The fluid velocity diminishes for magnifying the values of We because resistance to the flow is raised when impact of the elastic forces is less than the viscous forces ($We < 1$). The consistent elevation in temperature transverse to the cylindrical surface indicates that strong elastic effects encourage thermal diffusion in the viscoelastic coating i.e. the heat is efficiently propagated for amplifying the Weissenberg number (We). Therefore, the thermal boundary layer thickness is boosted for magnifying the values of We i.e. elastic forces is less than the viscous forces. It is to be noted that weak viscoelastic coatings ($We = 0.1$) attain higher fluid flow and lower heat transfer compared with strong viscoelastic coatings ($We = 0.7$). Although Weissenberg number generally represents the ratio of elastic forces to viscous forces in rheology, it has various manifestations in the non-Newtonian fluid dynamic literature. It may also be considered as the product of fluid relaxation time and shear rate. The Weissenberg number can also be used to quantify the orientation generated by the deformation or degree of anisotropy and is appropriate to characterise the flows with a constant stretch history and hence it can be utilized to express the rheology of smart

polymers. For $We = 0$, elastic effects become vanishingly small and purely viscous Newtonian flow is retrieved. The parameter values selected in Figs 5 and 6 are based on the established understanding that for $We \leq 1$ shear-thinning (pseudoplasticity) behaviour is exhibited in viscoelastic fluids, whereas for $We \geq 1$ shear-thickening (dilatant) behaviour is present. For $We = 1$ the elastic and viscous contributions are equivalent.

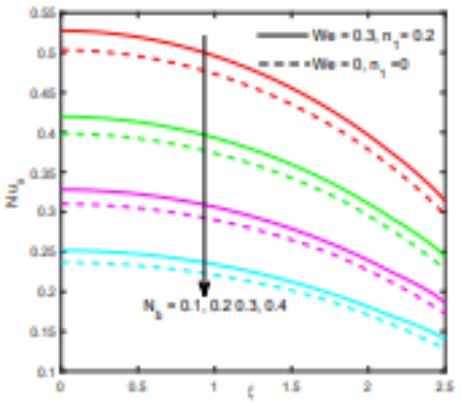

Fig. 25. Heat transfer rate profiles with various Brownian motion nanoscale numbers, Weissenberg numbers and tangent-hyperbolic power-law index parameter values.

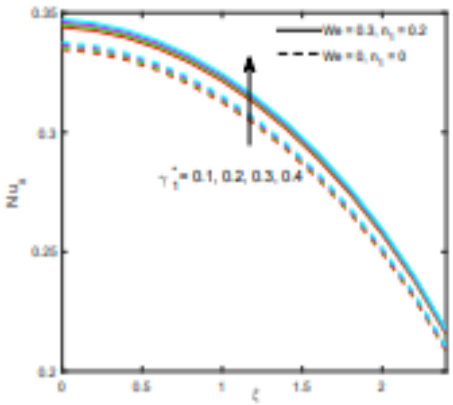

Fig. 26. Heat transfer rate profiles with various non-Fourier (thermal relaxation) numbers, Weissenberg numbers and tangent-hyperbolic power-law index parameter values.

Figures 7 and 8 depict the characteristic of n_1 on velocity and temperature distributions, respectively. Initially, an increment in n_1 values induces a notable decrease

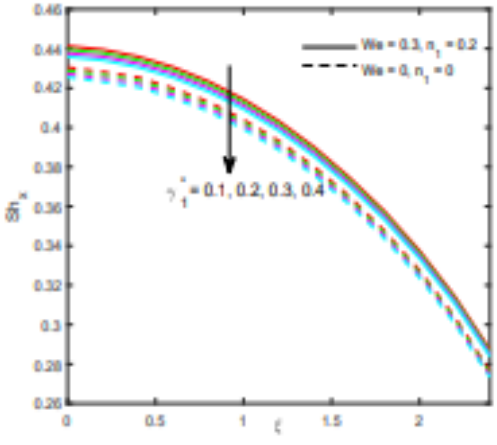

Fig. 27. Local Sherwood number distribution with various non-Fourier (thermal relaxation) numbers, Weissenberg numbers and tangent-hyperbolic power-law index parameter values.

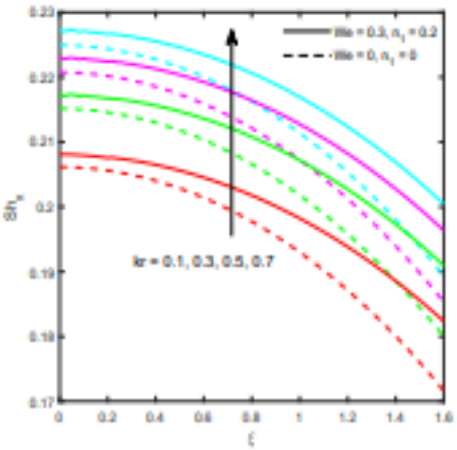

Fig. 28. Heat transfer rate profiles with various chemical reaction parameters, Weissenberg numbers and tangent-hyperbolic power-law index parameter values.

in velocities, and this is particularly prominent very near the surface of the cylinder ($\eta \sim 1$). However a reverse trend is elucidated further away from the surface of the cylinder. The parameter n_1 arises in the modified shear terms in the momentum boundary layer Eqn. (16). It represents the rheological power-law index in the tangent hyperbolic model. The Cauchy stress tensor of the tangent hyperbolic fluid is: $\bar{\tau} = \left[\mu_\infty + (\mu_0 - \mu_\infty)\tan\left(\Gamma\bar{\dot{\gamma}}\right)^{n_1}\right]$ Here, $\bar{\dot{\gamma}} = \sqrt{\frac{1}{2}\sum_i\sum_j \bar{\dot{\gamma}}_{ij}\bar{\dot{\gamma}}_{ji}} = \sqrt{\frac{1}{2}\Pi}$ where $\Pi = \frac{1}{2}tr\left(gradV + (gradV)^T\right)^2$. It is to be noted that the numerical computations can't be carried out when infinite shear rate viscosity is zero i.e., $\mu_\infty = 0$. Further, the pseudoplastic tangent hyperbolic fluid case is confined which depicts the shear thinning effects, i.e., $\Gamma\bar{\dot{\gamma}} < 1$. Based on these assumptions, the form $\bar{\tau} = \mu_0\left(\Gamma\bar{\dot{\gamma}}\right)^{n_1}\bar{\dot{\gamma}} = \mu_0\left[\left(1+\Gamma\bar{\dot{\gamma}}-1\right)^{n_1}\right]\bar{\dot{\gamma}} = \mu_0\left[\left(1+n_1\left(\Gamma\bar{\dot{\gamma}}-1\right)\right)\right]\bar{\dot{\gamma}}$ is adopted in the momentum boundary layer Eqn. (16). Here Γ is the time dependent material constant, $\bar{\dot{\gamma}}$ is the shear rate, and Π is the second invariant strain tensor. The values considered are $0 < n_1 < 1$ which correspond to pseudoplastic coating behaviour. Clearly, near the wall (surface of the cylinder) stronger pseudoplasticity induces deceleration whereas little away from the cylinder, the reverse trend is observed. This is connected to the relaxation of tensile stresses in the axial direction which induces a different effect depending on the location within the coating boundary layer, transverse to the cylindrical surface. Temperature is however consistently depressed since the stronger rheological behaviour (i. e. higher n_1 values) inhibits thermal diffusion in the regime and suppresses thickness of the thermal boundary layer. It is also noteworthy to mention that a very rapid decrement in profiles occurs from the wall to the free stream indicating that with stronger shear-thinning effect the boundary layer is cooled much more effectively compared with weakly pseudoplastic coatings. In combination with nanoscale properties (and micro-organism embedding), the pseudoplasticity can therefore be exploited to dissipate heat more quickly around the periphery of the cylinder and mitigate heat transmission, for example, a propulsion duct to the engulfing components of an aircraft engine. This technology may be of immense benefit to corporations specializing in thermal coating design for aerospace systems such as thermal insulation heat shields, for example, SA Thermal Engineering [76], Boeing Aerospace [77], etc.

Figures 9 and 10 visualize the effect of N_t on heat and mass transfer profiles, respectively. It is clear that both the temperature and nanoparticle concentration fields increase with an increment in N_t. The particle movement towards a colder zone due to the temperature gradient between the hot gas and the cold zone is known as thermophoresis. The nanoparticle distribution and variation in temperature are significantly controlled by the parameter (N_t). The temperature and nanoparticle concentration distribution of the nanofluid rise for magnifying the values of N_t and hence the boundary layer thicknesses of thermal and nanoparticle concentration (species) are augmented. An increase in N_t promotes the heat transfer away from the wall and this aggravates nanoparticle deposition away into the nanofluid region, increasing nanoparticle concentrations throughout the boundary layer in proximity to the surface of the cylinder, although the effect decays near the free stream. While the temperature distributions are homogenous throughout the region transverse to the wall, the nanoparticle concentrations exhibit a jump closer to the wall. This may be due to the intensity of motion closer to the surface of the cylinder which has been noted to be chaotic manifesting in non-homogenous distributions of nanoparticles in the boundary layer, as noted by Keblinski et al [78, 79]. Figures 11-13 show the influence of N_b on temperature, concentration and motile microorganism density number distributions, respectively. Brownian motion is amplified with increasing N_b and the

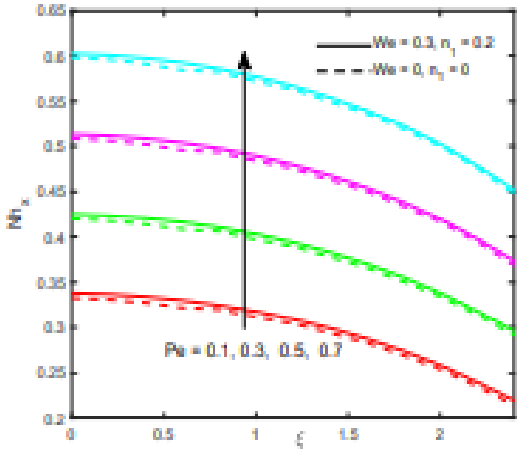

Fig. 29. Local gyrotactic micro-organism density number gradient profiles with bioconvection Peclet numbers, Weissenberg numbers and tangent-hyperbolic power-law index parameter values.

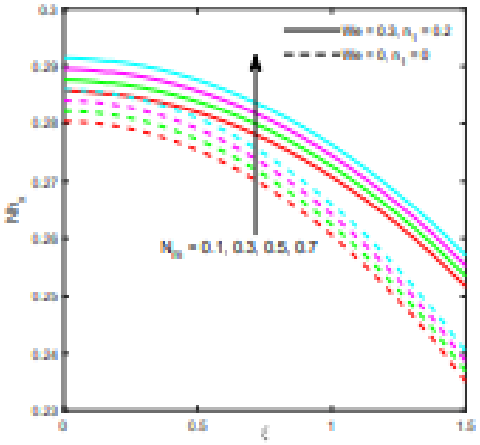

Fig. 30. Local gyrotactic micro-organism density number gradient profiles with microorganism concentration difference numbers, Weissenberg numbers and tangent-hyperbolic power-law index parameter values.

nanoparticles size is altered. It is to be noted that larger N_b values imply smaller nanoparticles. This encourages thermal diffusion via ballistic collisions which energizes the regime and elevates temperatures. Conversely, nanoparticle concentration magnitudes are suppressed since nanoparticle diffusion rate is reduced with stronger Brownian motion effect; the boundary layer thickness of nanoparticle species is also depleted. Similarly, while heat diffusion however is fortified with lesser nanoparticles (larger Brownian motion parameter values), the diffusivity of motile micro-organisms is reduced which manifests in a decrease in motile microorganism density number and boundary layer thickness of microorganism species. Therefore, to cool the coating and encourage a more homogenous migration of nanoparticles and micro-organisms, larger nanoparticles are required, and Brownian motion should be minimized.

The influence of non-Fourier (thermal relaxation) parameter γ_1^* on velocity and temperature profiles are depicted in Figures 14 and 15, respectively. It is ascertained that the thickness of momentum and thermal boundary layers reduce with higher values of γ_1^*. In case of finite-speed heat conduction, Fouriers law of heat conduction is physically realistic and is obtained when of $\gamma_1^* \to 0$. In this case the energy boundary layer Eqn. (16) reduces to the Fourier version: $\frac{\theta''}{P_r} + N_b\phi'\theta' + N_t\theta'^2 + f\theta' = \xi\left\{\frac{\partial\theta}{\partial\xi}f' - \frac{\partial f}{\partial\xi}\theta'\right\}$. For $\gamma_1^* > 0$, the so-called relaxation process results from the finite time necessary for molecules to diffuse between adjacent shearing layers in the medium. The adjacent (local) zone surrounding the nanoparticle highly influences the diffusion time of a nanoparticle. The random molecular diffusion nature is caused by the intrinsically heterogeneous features of real coatings. Higher values of non-Fourier (thermal relaxation) parameter therefore better approximate a finite speed of heat propagation. The result is that both velocity and temperatures are reduced with higher values of γ_1^*. The trends are sustained across the boundary layer transverse to surface of the cylinder. The momentum boundary layer thickness is therefore diminished while thickness of the thermal boundary layer is diminished.

Table 3. Variation in Cf_x, Nu_x, Sh_x, Nh_x at $\xi = 1$ for non-Newtonian bio-nano-coating (KBM and FEM solutions).

Parameter		$\xi = 1$							
		Cf_x		Nu_x		Sh_x		Nh_x	
		KBM	FEM	KBM	FEM	KBM	FEM	KBM	FEM
Ha	0.1	0.5215	0.5214	0.4178	0.4178	0.4805	0.4805	0.3497	0.3496
	0.3	0.4964	0.4963	0.4023	0.4022	0.4757	0.4757	0.3318	0.3317
	0.5	0.4754	0.4754	0.3885	0.3883	0.4727	0.4728	0.3176	0.3174
We	0.1	0.4736	0.4734	0.3894	0.3893	0.4726	0.4724	0.3179	0.3177
	0.3	0.4754	0.4752	0.3885	0.3887	0.4727	0.4727	0.3176	0.3174
	0.5	0.4771	0.4771	0.3877	0.3877	0.4729	0.4728	0.3174	0.3176
n_1	0.1	0.4937	0.4934	0.3780	0.3781	0.4745	0.4746	0.3150	0.3152
	0.3	0.4562	0.4561	0.4004	0.4002	0.4707	0.4709	0.3204	0.3206
	0.5	0.4126	0.4125	0.4295	0.4293	0.4650	0.4651	0.3263	0.3262
N	0.1	0.4935	0.4933	0.3780	0.3781	0.4747	0.4746	0.3152	0.3158
	0.3	0.4560	0.4560	0.4004	0.4002	0.4709	0.4707	0.3206	0.3204
	0.5	0.4124	0.4122	0.4295	0.4295	0.4652	0.4652	0.3265	0.3266
γ_1^*	0.0	0.4768	0.4765	0.3884	0.3886	0.4733	0.4737	0.3197	0.3198
	0.1	0.4754	0.4754	0.3885	0.3884	0.4727	0.4729	0.3176	0.3174
	0.2	0.4740	0.4743	0.3886	0.3886	0.4722	0.4722	0.3156	0.3156
N_t	0.1	0.4754	0.4752	0.3885	0.3883	0.4727	0.4728	0.3176	0.3178
	0.2	0.4906	0.4904	0.3269	0.3271	0.4825	0.4827	0.3289	0.3286
	0.3	0.5050	0.5050	0.2753	0.2753	0.5297	0.5297	0.3437	0.3437
N_b	0.1	0.4553	0.4553	0.4902	0.4902	0.3300	0.3304	0.2945	0.2948
	0.3	0.4943	0.4943	0.3025	0.3025	0.5180	0.5182	0.3312	0.3314
	0.5	0.5291	0.5291	0.1737	0.1737	0.5506	0.5508	0.3516	0.3517

The impact of Sc and Sb on mass transfer and density number of motile microorganism are illustrated in Figures 16 and 17. Evidently both nanoparticle concentration and motile microorganism magnitudes are decreased with larger Schmidt number and bioconvection Peclet number. Generally, mass diffusivity is inversely proportional to Schmidt number. Larger Sc values dilute the mass diffusivity and have the tendency to decrease the nanoparticle concentration. Higher concentration magnitudes are observed for gaseous diffusion in polymers ($Sc < 1$) because the species diffusion rate dominates the momentum diffusion rate. However, in the present scenario, metallic nanoparticles embedded in a rheological coating are assumed, for which $Sc > 1$ is considered; i.e. the species diffusion rate is dominated by the momentum diffusion rate and this will produce a depression in mass transfer profiles. When $Sc = 1$ the momentum and nano-particle species diffusion rates are equal and the thicknesses of the respective boundary layers are equivalent. The diffusivity of nanoparticles i.e. molecular species in the coating plays an important role in assuring the homogenous distribution of the nanoparticles throughout the coating and providing total as well as consistent protection to the cylinder. It is noteworthy that the species diffusion is assumed to obey Fickian diffusion, although in the future non-Fickian diffusion, which has also been reported in smart coating, may be examined. Of course, the present analysis is confined to laminar flow which is sustainable with the damping in the velocity field induced by radial magnetic field. This is contrary to ordinary spray deposition processes while faster are inherently turbulent and do not achieve the same degree of homogeneity of the coatings. Spray coating usually employs thermal (flame) deposition technology for metallic-based coatings, and this leads to heterogenous constitution of the final product which is not desirable for high tech applications in aerospace. The bioconvection number is a unique parameter where micro-organism dynamics occurs

simultaneously with momentum transfer. Whereas the ordinary Schmidt number Sc, expresses the ratio of momentum and nanoparticle species diffusivity, the bioconvection Schmidt number embodies the rate of momentum diffusion to micro-organism species diffusion. These two rates are rarely equal for the considered ($Sb \geq 1$) range of values. When $Sb = 1$ both diffusion rates are identical, and the motile (gyrotactic) micro-organism concentration (density number) is maximum. However, for $Sb > 1$ the micro-organism diffusivity is dominated by the momentum diffusivity and this leads to a depletion in propulsion of micro-organisms in the coating. The boundary layer thickness of micro-organism species is therefore diminished for increasing the bioconvection Schmidt number. Overall, both mass diffusivity of nanoparticles and species diffusivity exert a substantial influence on diffusion characteristics in the coating.

Figures 18 and 19 present the effects of Pe and N_m on motile micro-organism profiles. It is observed that magnifying the values of Pe and N_m diminish Ψ. Both parameters arise in the same clustered term, $-\frac{Pe}{Sb}\left[\phi''\left(N_m + \Psi\right) + \phi'\Psi'\right]$ in the micro-organism species boundary layer. As noted by Pedley and Kessler [56], Zohra et al. [63], and Aneja et al. [65], bioconvection Peclet number (Pe) is a critical parameter in propulsion dynamics of micro-organisms for smart coatings. It is to be noted that $Pe = bW_c/D_n$ and therefore Pe expresses the impact of diffusivity of micro-organisms (D_n), maximum swimming speed of micro-organism (W_c) and chemotaxis constant (b). The motile micro-organism flow patterns considerably vary for varying the Pe as elucidated in Fig. 18. The concentration of microorganisms dilutes for amplifying the Peclet number because microorganisms propel faster with higher microorganisms swimming speed. Alternatively, the micro-organism concentration in the nanofluid boundary layer rises for decreasing the values of Peclet number because mobility of the micro-organisms diminishes for lower values of Peclet number. $N_m = \frac{N^*}{N_w - N_\infty}$ is the micro-organism concentration difference variable and this augments the micro-organism diffusion term, $\phi''\left(N_m + \Psi\right)$. Although micro-organisms propel more efficiently with larger N_m, the distribution is reduced i.e. gyrotactic micro-organisms concentration is reduced and the associated species boundary layer thickness is depleted.

Figures 20-30 present the distributions for skin friction (local cylindrical surface shear stress), local Nusselt number, local Sherwood number and local motile micro-organism density number wall gradient, with axial (stream wise) coordinate, ξ. Figures 20-22 show the influence of Ha, N_t and N_b on skin friction coefficient for both non-Newtonian and Newtonian cases. It is clear from these figures that friction factor consistently enhances with increasing values of axial coordinate till $\xi \approx 1.7$ and then friction factor diminishes. Results reveal that skin friction rises with magnifying values of N_t and N_b while it declines for amplifying values of Ha. Further, it is noticed from these figures that the friction factor values of Newtonian fluid is higher compared with non-Newtonian fluid. Figures 23-26 visualize the impact of Ha, N_t, N_b and γ_1^* on local heat transfer rate. Nusselt number, decreases for larger values of Brownian motion parameter, thermophoresis parameter, and magnetic field parameter but the reverse behaviour is detected for larger values of γ_1^*. It is pertinent to note that using the Fourier model leads to an under prediction in local Nusselt number to the surface of the cylinder i.e. over-prediction in temperatures. It is observed from Fig. 26 that adopting the non-Fourier model with thermal relaxation, provides better accuracy compared with the Fourier model. Figures 27 and 28 illustrate the sherwood number variation for γ_1^* and Kr, respectively. It is apparent from these figures that the local sherwood number lessens for higher values of γ_1^* whereas it elevates with higher values of Kr. In general, the chemical reactions are majorly

classified into two types, namely heterogeneous chemical reactions and homogeneous chemical reactions. Chemical changes occurring with gases or liquids depend on the type of interactions of these chemical substances. Homogeneous reactions happen in single stage only whereas heterogeneous reactions happen in at least two phases. For destructive homogenous reactions, as considered here, nanoparticles react to produce a different species. Figures 29 and 30 show the variation of motile micro-organism density gradient with stream wise coordinate for different values of Pe and N_m, respectively. An increment in both parameters (motile micro-organism concentration difference (N_m) and bioconvection Peclet number (Pe)) elevates the rate of transfer of gyrotactic micro-organisms in the surface of the cylinder.

The numerical values of friction factors, heat transfer rate, local Sherwood number and microorganism density number gradient for tangent hyperbolic non-Newtonian fluid are shown in Table 3. It is noticed that the friction factor is boosted with an elevation in Weissenberg number (We), Brownian parameter (Nb) and thermophoresis parameter (Nt) whereas the contrary response is detected with an increment in Hartmann magnetic number (Ha), tangent hyperbolic power-law rheological index (n_1), non-Fourier thermal relaxation parameter (γ_1^*) and buoyancy ratio parameter (N) (ratio of thermal and nanoparticle solutal buoyancy forces). It is noteworthy that higher We value implies a larger relaxation time, which in turn produces higher associated tensile stresses in the coating. This accelerates the coating flow and results in a boost in skin friction factor. Local Nusselt number intensifies with higher values of n_1, γ_1^*, and N, whereas it suppresses with larger values of Hartmann magnetic number (Ha) i.e. stronger radial magnetic field. Mass transfer rate increases with an increase in We, N_t and N_b. Density number of motile microorganism gradient enhances with boosting values of n_1, N_t, and N_b; indicating that a more intense migration of gyrotactic micro-organisms arises from the boundary layer coating regime to the surface of the cylinder. It is observed from this table that the results obtained by using the Keller box method code and SMART-FEM code are similar for all the considered effects.

7 Conclusion

Motivated by developments in novel biological nano-smart coating technologies for the aerospace, naval and medical industries, in this article, axisymmetric magnetohydrodynamic gyrotactic bioconvection flow of a tangent-hyperbolic pseudoplastic non-Newtonian nanofluid from a cylindrical surface immersed in a Darcy porous medium with chemical reaction, is analyzed. The impact of Cattaneo-Christov heat flux (non-Fourier thermal relaxation parameter), Brownian motion and thermophoresis are taken into consideration. The tangent hyperbolic model is deployed for nanofluid rheology. The steady-state partial differential conservation boundary layer equations are rendered dimensionless via appropriate transformations and the resulting coupled, nonlinear two-parameter partial differential boundary value problem is solved computationally with the second order accurate, implicit Keller box method and the results are illustrated graphically. The effect of pertinent parameters such as modified Hartmann magnetic number, Weissenberg viscoelastic parameter, non-Fourier thermal relaxation parameter, Brownian motion, thermophoresis, Schmidt number, chemical reaction parameter, micro-organisms concentration difference variable, bioconvection Peclet number and bio-convection Schmidt number on the flow, heat transfer, mass transfer, motile density, local skin friction, heat transfer rate, nanoparticle mass transfer rate and local microorganism density number wall gradient is visualized graphically. Validation with earlier studies is included. Further validation with

a variational finite element method code (SMART-FEM) is also presented. The key findings of the present investigation are as follows:

- The temperature of tangent hyberbolic nanofluid coating decreases with increasing values of non-Fourier (thermal relaxation) parameter.
- Very near the surface of the cylinder ($\eta \sim 1$), tangent hyberbolic nanofluid coating velocity decreases with higher values of the pseudoplastic power law index parameter whereas a reverse trend is elucidated further away from the surface of the cylinder.
- The concentration of gyrotactic motile micro-organism number density is decreased with an increment in bioconvection Peclet number and microorganisms concentration difference parameter.
- Heat transfer rate is suppressed with boosting values of Hartmann magnetic parameter (radial magnetic field), thermophoresis parameter and Brownian motion parameter.
- Magnifying the chemical reaction parameter amplifies the mass transfer rate.

The present study has neglected electromagnetic induction effect. These may be considered in future studies.

References

1. K. C. Chang and J. M. Yeh, Intelligent Coatings for Corrosion Control, (2015).
2. M. D. Shamshuddin, S. R. Mishra, O. Anwar Beg, T.A. Beg and Ali Kadir, Heat Transfer (2020). *DOI: 10.1002/htj.21963.*
3. Intelligentmaterial.com/IMS Intelligent Material (2020).
4. A. S. Butt, A. Ali , S. Munawar, Int. J. Exergy, **13(1), 1 (2013)**
5. N. Saleem, S. Munawar, International Journal of Bio mathematics, **9(2),1650027 (2016)**
6. D. E. Weidner, J. Magnetism and Magnetic Materials, **489**, 165352 (2019).
7. W. Chen, T. Long, Y. J. Guo, Z. A. Zhu, Y. P. Guo, Journal of Materials Chemistry B, **12**, 1653 (2014).
8. T. Cheng, R. He, Q. Zhang, X. Zhan, F. Chen, Journal Materials. Chemistry A, **3**, 21637 (2015).
9. F. Xia, W. Yue, J. Wang, C. Liu, F. Wang, Y. Li, Ceramics International: A, **41(9)**, 11445 (2015).
10. S. H. Teh and I. I. Yaacob, IEEE Transactions on Magnetics, **47(10)** 4398 (2011).
11. J. Halim, R. Abdel-karim, S. Raghy, M. Nabil, A. Waheed, Journal of Nanomaterials, (2012).
12. T. Tang, Y. Fu, Coatings, **10**, 51 (2020).
13. H. Wang, T. Chen, W. Cong, D. Liu, Coatings, **9**, 109 (2019).
14. S. Vorobyev, E. Vishnyakova, M. Likhatski, A. Romanchenko, I. nemtsev, Y. Mikhlin, Nanomaterials, **9(11)**, 1525 (2019).
15. D. He, S. Grag, T.D, Waite, Langmuir, **28**, 10266 (2012).
16. L. Feng, G. Gao, P. Huang, X. Wang, C. Zhang, J. Zhang, S. Guo, D. Cui, Nanoscale Res. Lett., **6**, 551 (2011).
17. L. E. Murr, Springer, USA (2015).
18. M. Kumar, Y. Ando, J. Nanosci. Nanotechnol., **10**, 3739 (2010).
19. ssnano.com/ (2020) [SkySpring Nanomaterials, Houston, Texas, USA]
20. S. K. Das, S. U. Choi, W. Yu, T. Pradeep, Nanofluids: Science and Technology; John Wiley and Sons: Hoboken, NJ, USA (2007).
21. R. Jafari, L. F. Mobarakeh, M. Farzaneh, Nano Sci. Technol. Lett. 4, 369374 (2012).
22. W. Jiang , L. SheN, K. Wang, Z. Wang, Z. Tian, Proc. IMechE- Part B: Journal of Engineering Mamufacture, **234**, 431 (2019).
23. M. Tajbakhsh, O. Yaghbizadeh, M. Farhadi Nia, Proc. IMechE- Part E: Journal of Process Mechanical Engineering, **233**, 94 (2017).

24. J. Buongiorno, ASME J. Heat Transfer, **128**, 240, (2006).
25. J. Koo, NC State University, Raleigh, NC, USA (2004).
26. J. Li, NC State University, Raleigh, NC, USA (2008).
27. R. K. Tiwari , M. K. Das, International Journal of Heat and Mass Transfer, **50**, 2002 (2007).
28. O. Anwar Beg, A. Subba Rao, N. Nagendra, C. H. Amanulla, M. Surya Narayana Reddy and A. Kadir, J. Nanofluids, **7**,1 (2018).
29. N. Shukla, P. Rana, O. Anwar Beg, Bani Singh and A. Kadir, Propulsion and Power Research (2019).
30. S. A. Gaffar, V. Ramachandra Prasad and O. Anwar Beg, Int. J. Appl. Comput. Math., **1**, 651 (2015).
31. M. Y. Malik, T. Salahuddin, A. Hussain, S. Bilal, J. Magn. Magn. Mater. **395**, 271 (2015).
32. K. Ganesh Kumar, B. J. Gireesha, M. R. Krishanamurthy, N. G. Rudraswamy, Results Phys., **7**, 3031 (2017).
33. T. Hayat, M. Shafque, A. Tanveer, A. Alsaedi, Int. J. Heat Mass Transf. **102**, 54 (2016).
34. S. A. Gaffar, V. R. Prasad, E. Keshava Reddy and O. Anwar Beg, Arabian Journal for Science and Engineering, **39**, 8157 (2014).
35. H. T. Basha, R. Sivaraj, V. R. Prasad, O. Anwar Beg, J. Thermal Analysis and Calorimetry (2020).
36. S. A. Gaffar, V. Ramachandra Prasad, S. Keshava Reddy, O. Anwar Beg, J. Braz. Society Mech. Sci. Eng., **39**, 101 (2017).
37. P. R. Reddy, S. Abdul Gaffar, B. Md. Hidayathulla Khan, K. Venkatadri and O. Anwar Beg, Heat Transfer (2020). *DOI: 10.1002/htj.22011*.
38. L. Pawlowski, Second Edition, John Wiley and Sons, New York, USA (2008).
39. J. B. J. Fourier, Chez Firmin Didot, Paris (1822).
40. C. Cattaneo, Atti del Seminario Matematico e FisicodellUniversita' di Modena, **3**, 83 (1948).
41. C. I. Christov, Mechanics Research Communications, **36**, 481486 (2009).
42. B. Straughan, International Journal of Heat and Mass Transfer, **53**, 2808 (2010).
43. B. Straughan, International Journal of Heat and Mass Transfer, **53**, 95 (2010).
44. S. Han, L. Zheng, C. Li, X. Zhang, Applied Mathematics Letters, **38**, 87 (2014).
45. S.R. Mishra, M. Shamshuddin,O. Anwar Beg, Ali Kadir, Heat Transfer, **48(1)**, 435 (2019).
46. V. Tibullo, V. A. Zampoli, Mechanics Research Communications, **38**, 77 (2011).
47. R. Mehmood, S. Rana, O. Anwar Beg and A. Kadir, J. Brazilian Soc. Mech Sci. Eng. (2018). *https:doi.org/10.1007/s40430-018-1446-4*.
48. J. A. Khan, M. Mustafa, T. Hayat, A. Alsaedi, PLoS One, **10**, e0137363 (2015).
49. S. R. Mishra, M. D. Shamshuddin, O. Anwar Beg and A. Kadir, Arabian J. Science Engineering (2019). *doi.org/10.1007/s13369-019-04019-x*.
50. T. Hayat, M. Imtiaz, A. Alsaedi, S. Almezal, Journal of Magnetism and Magnetic Materials, **401**, 296 (2016).
51. F. A. Elsayed, O. Anwar Beg, J. Mechanics Medicine Biology, **14**, 3 (2014).
52. H. Wager, Philos Trans R Soc Lond B, **203**, 333 (1911).
53. J. R. Platt, Science, **133**, 1766 (1961).
54. T. J. Pedley, N. A. Hill, J. O. Kessler, J. Fluid Mech. **195**, 223 (1988).
55. A. V. Kuznetsov, Int. Comm. Heat Mass Transfer, **32**, 991 (2005).
56. T. J. Pedley, J. O. Kessler, Ann. Rev. Fluid Mech., **24**, 313 (1992).
57. D. E. Weidner, Physics of Fluids, **29**, 052103 (2017).
58. G. Janardhana Reddy, Bhaskerreddy Kethireddy, O. Anwar Beg, Int. J Mechanical Sciences, **140**, 493 (2018).
59. M. D. Shamshuddin, M. Ferdows, Rezwan, O. Anwar Beg, A. Kadir, Proceedings of the International Conference on Numerical Heat Transfer and Fluid Flow (NHTFF-2020), NIT Warangal, 17 (2020).
60. J. Zueco, O. Anwar Beg, Tasveer A. Beg and H. S. Takhar, J. Porous Media, **12**, 519 (2009).

61. Md Faisal Md Basir, M.J. Uddin, A. I. Md. Ismail and O. Anwar Beg, AIP Advances, **6**, 055316-1 (2016).
62. S. Siddiqa, M. Sulaiman, M.A. Hossain, S. Islam, R.S. Gorla, Int. J. Therm. Sci., **1 (108)**, 244 (2016).
63. F. T. Zohra, M.J. Uddin and A.I. Ismail, O. Anwar Beg and A. Kadir, Chinese J. Physics, **56**, 432 (2018).
64. P. Sudhagar, P. K. Kameswaran, B. R. Kumar, ASME J. Therm. Sci. Eng. Appl. **11(4)** (2019).
65. M. Aneja, Sapna Sharma, S. Kuharat, O. Anwar Beg, Int. J. Modern Physics B, **33**, 2050028 (2020).
66. J. H. Merkin, ASME J. Heat Transf. **99(3)**, 453 (1977).
67. R. Nazar, N. Amin, I. Pop, Proceeding of the 12th International Conference (2002).
68. J. N. Reddy, MacGraw-Hill, New York (1985).
69. S. Rawat, R. Bhargava, Renu Bhargava and O. Anwar Beg, Proc.IMechE Part C- J. Mechanical Engineering Science, **223**, 2341 (2009).
70. P. Rana, R. Bhargava and O. Anwar Beg, Computers and Mathematics with Applications, **64**, 2816 (2012).
71. O. Anwar Beg, Tasveer A. Beg, R. Bhargava, S. Rawat and D. Tripathi, J. Mechanics in Medicine and Biology, **12(4)**, 1250081.1 (2012).
72. P. Rana, R. Bhargava and O. Anwar Beg, Proc. IMECHE- Part N; J. Nanoengineering and Nanosystems, **227**, 77 (2013).
73. P. Rana, R. Bhargava, O. Anwar Beg and A. Kadir, Int. J. Applied Computational Mathematics, **3(2)** 1421 (2017).
74. O. Anwar Beg, R. Bhargava, S. Sharma, Ali Kadir, Tasveer A. Beg, M. Shamshuddin, Computational Thermal Sciences, **12(1)**, 79 (2020).
75. N. Mukhin, I. Sokolova, D. Chigirev, L. Rudaja, G. Lebedeva, R. Kastro, M. Bolshakov, M. P. Schmidt, S. Hirsch, Coatings, **10(3)**, 286 (2020).
76. Thermal engineering.co.uk (SA Thermal Engineering- coatings) (2020).
77. Boeing distribution.com Boeing Aerospace - coatings, Washington, USA (2020).
78. P. Keblinski, Materials Research Society Spring Symposium, New York, USA, (2007)
79. P. Keblinski, S. R. Phillpot, S. U. S. Choi, J. A. Eastman,International Journal Heat Mass Transfer, **45(4)**, 855 (2002).